WATER RESOURCES RESEARCH, VOL. 49, 4157–4173, doi:10.1002/wrcr.20330, 2013

On the formation of breakthrough curves tailing during convergent flow tracer tests in three-dimensional heterogeneous aquifers

D. Pedretti,[1] D. Fernàndez-Garcia,[1] D. Bolster,[2] and X. Sanchez-Vila[1]

Received 27 November 2012; revised 4 May 2013; accepted 27 May 2013; published 22 July 2013.

[1] Anomalous transport in advection-dominated convergent flow tracer tests can occurs due to small-scale heterogeneities in aquifer hydraulic properties. These result in fluctuations of the groundwater velocity field and complex connectivity patterns between injection and extraction wells. While detailed characterization of heterogeneity is often not possible in practice, a proper understanding of what fundamental physical mechanisms can give rise to macroscopic behaviors that are measurable is essential for proper upscaling of solute transport processes. We analyze here how heavy-tailed breakthrough curves can arise in radially convergent flow to a well. The permeability fields are three-dimensional multi-Gaussian fields with varying statistical geometry and degrees of heterogeneity. We consider transport of conservative tracers from multiple injection locations by varying distance and angle from the extraction well. Anomalous power law tailing in breakthrough curves is attributed to a variety of features including the initial vertical stratification of the solute that arises due to a flux-weighted injection, the injection distance to the well relative to the depth of the aquifer, and the statistics of the heterogeneity field as defined by the correlation length and variance of the permeability. When certain conditions cooccur for a given injection, such as strong connectivity contrasts between aquifer layers, injection distances comparable to the horizontal heterogeneity integral scales, and large global variances, breakthrough curves tend to scale as a PL with unit slope at late time. These findings offer new insights to understand what physical processes must be understood to develop and choose appropriate upscaling approaches that might reproduce such anomalous transport in heterogeneous advection-dominated systems.

Citation: Pedretti, D., D. Fernàndez-Garcia, D. Bolster, and X. Sanchez-Vila (2013), On the formation of breakthrough curves tailing during convergent flow tracer tests in three-dimensional heterogeneous aquifers, *Water Resour. Res.*, *49*, 4157–4173, doi:10.1002/wrcr.20330.

1. Introduction

[2] Transport parameters are often obtained from interpreting the temporal evolution of concentrations at a given location or volume control section (breakthrough curves (BTCs)). The actual estimated parameters are model dependent. The conventional approach based on the advection-dispersion equation (ADE) [*Bear*, 1972] has been shown consistently to fail at completely predicting data obtained from real sites. In such cases, transport is called "anomalous" or non-Fickian. Many authors have postulated that non-Fickianity is a consequence of the presence of heterogeneity in hydraulic parameters [e.g., *Levy and Berkowitz*, 2003; *Salamon et al*., 2007; *Riva et al*., 2008].

[3] Phenomenological evidence of this effect of heterogeneity comes from observations of heavy-tailed distributions on BTCs [e.g., *Hoehn et al*., 1998; *Fernàndez-Garcia et al*., 2004; *Gouze et al*., 2008]. Sometimes, BTC tails at late times scale like power laws (PLs) of the form $c \sim t^{-m}$ (long after the peak is observed). The parameter m is often called the "BTC slope" since PL distributions scale as straight lines in double log plots; in the literature m has been reported to range anywhere between one and three [e.g., *Becker and Shapiro*, 2000, 2003; *McKenna et al*., 2001].

[4] A general current goal is to find strict relationships between PL-shaped BTCs and specific spatiotemporal distributions of physical soil properties [e.g., *Dentz and Berkowitz*, 2003; *Bijeljic and Blunt*, 2006; *Willmann et al*., 2008; *Dentz and Bolster*, 2010]. In this paper, our aim is to show that heavy-tailed BTCs with PL late-time distributions can be found in finite-scale stationary hydraulic conductivity, K, fields, provided a third spatial dimension is accounted for and flow is convergent to a well.

[5] Convergent flow appears naturally in describing many flow configurations from real experiments. In fact, the most common form of tracer test is perhaps the convergent

[1]Hydrogeology Group, Department of Geotechnical Engineering and Geo-Sciences, Universitat Politècnica de Catalunya, UPC-BarcelonaTech, Barcelona, Spain.

[2]Department of Civil Engineering, University of Notre Dame, Notre Dame, Indiana, USA.

Corresponding author: D. Pedretti, Hydrogeology Group, Department of Geotechnical Engineering and Geo-Sciences, Universitat Politècnica de Catalunya, UPC-BarcelonaTech, C/Jordi Girona 1-3, Ed.D2/004/01, Barcelona ES-08034, Spain. (daniele.pedretti@upc.edu)

0043-1397/13/10.1002/wrcr.20330

flow tracer test (CFTT). This is for practical reasons, such as a better control of test duration, reduced required tracer mass and large mass recoveries (compared, for example, with natural-gradient flow tracer tests).

[6] Classical examples of stationary fields include multi-Gaussian fields with log-transformed hydraulic conductivity. One of the conclusions in *Willmann et al*. [2008] is that no PL-shaped late-time behavior of BTCs could be observed from transport through 2-D stationary multi-Gaussian fields, unless an artificial modification of the conductivity field was made. Nonetheless, the presence of heavy-tailed BTCs for short travel distances in multi-Gaussian fields with log-transformed hydraulic conductivity (called Y field, where $Y = \ln(K)$) was shown by *Sanchez-Vila and Carrera* [2004] using 1-D analytical and numerical solutions.

[7] An example of BTCs that can be observed in heterogeneous media was given by *Fernàndez-Garcia et al*. [2004], who experimentally studied convergent, divergent, and uniform flow tracer tests in an intermediate-scale three-dimensional heterogeneous aquifer constructed in the laboratory with different types of sands. The resulting K distribution showed correlated structures, well described by an exponential variogram model. Several conservative (bromide) and sorptive (lithium) tracers were injected at different points located between one and five horizontal integral scales from the extraction well. Concentrations were recorded as depth-integrated BTCs. Four of the experimental BTCs obtained during the CFTTs using a deep-penetration source injection [*Fernàndez-Garcia*, 2003] are shown in Figure 1 and clearly display nonuniform transport behavior. We observe that (a) the BTC obtained from injecting at E1 (located two integral scales away from the pumping well) displayed a heavy-tailed distribution after the peak, well approximated by a PL with $m = 1$; (b) at the same radial distance from the pumping well, the BTCs obtained from injections at E2 and E3 were less anomalous and quite symmetric; and (c) E4, also at the same injection distance, is much more irregular and only approximately similar to a PL with $m = 1$.

[8] These results lead us to ask the following questions: Does scaling in BTCs with a PL with $m = 1$ occur for some specific physical reasons, or is it just a random output? More generally, are there any, and if so what are the physical mechanisms controlling BTC scaling, for large time after injection in radial convergent flow?

[9] *Willmann et al*. [2008] tried to answer to the latter question, using 2-D numerical simulations to reproduce anomalous transport under the assumptions of uniform flow conditions and finite correlated heterogeneous log conductivity fields (i.e., fields with log-normally distributed hydraulic conductivity). They concluded that classical low-order geostatistical indicators (such as variograms), usually adopted to characterize these fields, cannot be directly related to parameters associated with anomalous transport models such as those including memory functions [*Carrera et al*., 1998]. Similar results were also found by *Flach* [2012], who used dual-domain models.

[10] According to *Zinn and Harvey* [2003] and *Willmann et al*. [2008], among others, connectivity is the hydrodynamic parameter that most influences BTC late-time behavior. Here connectivity is defined as the ratio between spatially averaged and effective parameters defining flow and transport [*Knudby and Carrera*, 2006]. We refer to the recent work by *Renard and Allard* [2013] for an extensive review of connectivity concepts.

[11] In the simulations of *Willmann et al*. [2008], the BTC slopes were bounded by a minimum value of $m \approx 2$, which is not in agreement with the experimental observations reported by *Fernàndez-Garcia et al*. [2004]. It is not truly fair though to compare these works for two main reasons. First, radially converging flow is fundamentally different from uniform flow. For instance, tailing can naturally arise in BTCs, even for homogeneous fields [*Gelhar and Collins*, 1971; *Moench*, 1989; *Welty and Gelhar*, 1994]. Second, 2-D models are not suitable to reproduce this type of CFTT, where the distance between injection and controlling section is on the range of the representative heterogeneity scale such as the integral scale (I) in a multi-Gaussian K field. In this case, whenever possible, 3-D models are preferable [e.g., *Dagan*, 1989].

[12] Dimensionality is also a key factor when studying connectivity. Inclusion models [e.g., *Fiori et al*., 2006] show, for instance, that nonsymmetric BTCs naturally arise from the distribution of travel times in 3-D models under uniform flow; moreover, this method also showed that (flow) connectivity is largely enhanced by 3-D configurations relative to their 2-D counterparts [*Fiori and Jankovic*, 2012]. This is particularly true if unconditional sequential Gaussian simulations (SGSs) are used to simulate stochastic hydraulic conductivity fields [*Fernàndez-Garcia et al*., 2010]. In fact, *Willmann et al*. [2008] had to heavily condition their simulations to generate highly conductive nonstationary structures that gave rise to heavy-tailed BTCs similar to those observed in the field. It should be noted that the numerical 3-D flow and transport simulations by *Fogg* [1986] showed that one of the most influential factors controlling flow and transport is the connectivity of lenses, rather than the relative K value of the lenses themselves. The reliability of 2-D SGS to adequately reproduce transport connectivity patterns has been extensively debated in the past [e.g., *Sanchez-Vila et al*., 1996; *Gomez-Hernandez and Wen*, 1998]; however, 3-D models have received much less study, in large part due to the still highly computationally intensive nature of 3-D simulations.

[13] In this paper, we investigated the origin and development of heavy-tailed BTCs using 3-D numerical realizations under radially convergent flow conditions. We simulated synthetic heterogeneous fields drawn from a multi-Gaussian log-normal K distribution. Such a distribution is characterized by different combinations of finite-scale correlation and variances. Our aim was to provide new insights to explain how and why BTCs behave in typical CFTT field settings. We also aimed to find the key physical links to interpret the results obtained from field tracer tests in real applications.

[14] This paper is structured as follows. In section 2, we described the numerical approach we used to reproduce CFTTs in synthetic heterogeneous aquifers. Section 3 shows the results in which we highlighted how BTC tailing develops in different heterogeneous fields. This paper ends with a final discussion on the similarities between 3-D simulations and their corresponding 2-D counterparts, the role of the local dispersivity, and a possible physical

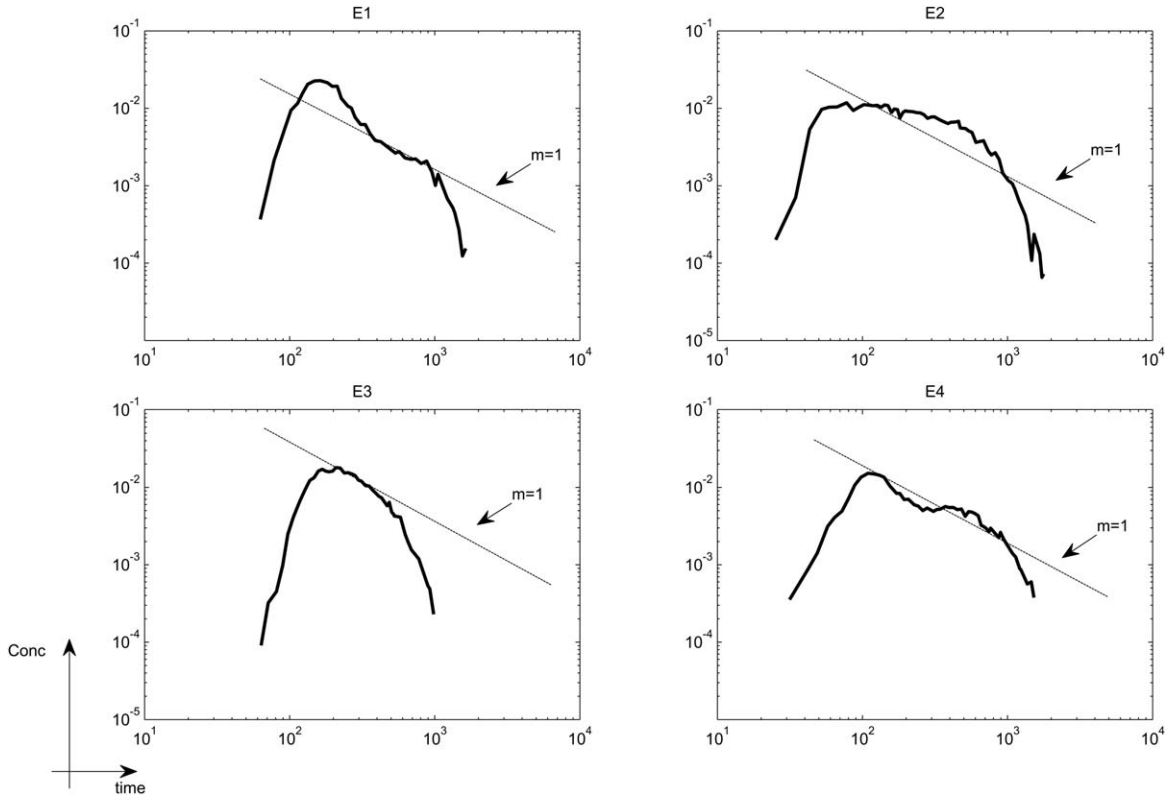

Figure 1. Four of the experimental BTCs obtained by *Fernàndez-Garcia et al*. [2004] during CFTT in heterogeneous 3-D tank. Notice that the part of the BTCs showing heavy-tailed distribution scale following $c \sim t^{-1}$ (at E1 and at E4), while at E2 and E3 the shape is more symmetric. The injecting location varies within the 3-D tank, keeping the radial distance from the well $(r_\lambda \approx 2)$

explanation of PL scaling on the BTCs, in section 4, and the conclusions.

2. Numerical Simulation of CFTT in Different Geological Settings

[15] We considered a typical CFTT scenario, in which a passive injection well (or piezometer) is located at a distance (r) from an extraction well. We assumed both wells to be fully penetrating the aquifer, which is confined and characterized by constant thickness (b). The extraction well is activated to withdraw groundwater at a constant discharge rate (Q). Once steady-state conditions are established at the injection well, a known mass (M) of tracer is introduced into the aquifer through the injection well. Under ideal conditions the injected mass is fully recoverable. In real field tests, a combination of mass losses and finite recording times leads to partial recovery of the injected mass.

[16] In heterogeneous aquifers, under forced-gradient conditions, the horizontal flow velocity can vary along the vertical column by several orders of magnitude. This variability depends on the hydraulic disorder of the system (described, for instance, by variance of Y, σ_Y^2 which can vary from $\sigma_Y^2 = 0.1 - 1$ for mildly heterogeneous systems to $\sigma_Y^2 > 4$ for highly heterogeneous ones [e.g., *MacKay et al*., 1986; *Bohling et al*., 2012]); it can also depend on local hydraulic gradients, which are controlled, for instance, by well pumping rate Q. Therefore, the amount of tracer mass injected into the aquifer at different depths is proportional to the local horizontal velocity found at the different horizons along the vertical injection column. This configuration forces one to pose the problem in terms of "flux-averaged" concentration rather than resident ones [e.g., *Parker and Van Genuchten*, 1984].

[17] BTCs can be measured both at the extraction well and if possible, at some control section between the injection and the extraction location. We assumed that only the extraction well is used for measuring concentrations. At the extraction well, concentrations are usually observed as "depth-integrated" measures over the entire screened section of the well, taking samples of the water once withdrawn and pushed to the surface. Alternatively, measurements can be made at different intervals along the screened section of the well, for instance, using "clustered columns," or "packers" [e.g., *Ptak et al*., 2004]. While "depth-integrated" BTCs are more commonly and easily obtained in the practice, "multilayered" BTC can provide useful information about stratification of transport properties of the aquifers, can provide valuable potential information about mixing [e.g., *Le Borgne et al*., 2010; *Bolster et al*., 2011], and can help indicate the existence of preferential flow paths [e.g., *Ptak and Schmid*, 1996; *Bianchi et al*., 2011].

[18] With these concepts in mind, we adopted a classical numerical approach consisting of

[19] (1) generation of a number of 3-D realizations of log hydraulic conductivity Y fields from a predefined geostatistical model;

[20] (2) solution of the groundwater flow problem in each of the Y fields by setting appropriate boundary conditions to impose forced-gradient behavior to a well;

[21] (3) solution of the transport problem by means of a random-walk particle method; and

[22] (4) calculation of BTCs, both as "depth-integrated" and "multilevel" concentrations at the well.

[23] Details of the different steps are provided in the subsequent subsections.

2.1. Simulation of Heterogeneous Hydraulic Conductivity Fields and Convergent Flow Solution

[24] We started by generating three stochastic realizations of Y fields using a SGS algorithm included in the Stanford geostatistical modeling software (SGEMS) [*Remy et al.*, 2009]. The support grid consisted of a regular 3-D lattice composed of $N_L = 100$ planar layers, each of which was made up of $N_C = 251$ horizontal square cells per side. We used i, j to identify a cell, respectively, in the x, y direction $(i,j = 1, \ldots, N_C)$ and k to identify a specific layer $(k = 1, \ldots, N_L)$. We assumed Y to be isotropic in each cell, with the exception of the central vertical column, which represented the well. Here we imposed very large vertical conductivities. Each cell has unit size, in all three directions (i.e., $r = 1$ corresponds to 1 cell).

[25] By construction, all Y fields had zero mean log-transformed hydraulic conductivity $\left(\overline{Y} = 0\right)$. Three exponential variograms with unit variance $\left(\sigma_Y^2 = 1\right)$ and variable integral scales (I) were used. Thus, denoting the three directional integral scales as I_x, I_y, and I_z, we built

[26] (1) Field (A): $I_x = I_y = I_z = 4$;

[27] (2) Field (B): $I_x = I_y = 40$, $I_z = 4$;

[28] (3) Field (C): $I_x = I_y = I_z = 40$.

[29] Field (B), reported on the left of Figure 2, displays statistical axisymmetric anisotropy, with ratios $I_x = I_y$ and $I_x/I_z = I_y/I_z = 10$. Fields (A) and (C) are statistically isotropic, but with different integral scales to explore the impact of the relative distance of the injection point. Note that the same fields will be used throughout to explore the effect of having larger variances (increased degree of heterogeneity) by simple scaling of the variance. For this reason, Figure 2 does not report a color legend.

[30] To obtain pumping conditions in each heterogeneous field, we proceeded as follows. In each realization and at each cell, Y were back-transformed to arithmetic values $(K = \exp(Y))$, and set as the hydraulic conductivity within the finite-difference numerical code Modflow-2000 [*Harbaugh et al.*, 2000]. Flow simulations were run under steady-state conditions, and the aquifer was considered confined. To simulate radial flow conditions, we set Dirichlet boundary conditions at the lateral domain sides and assigned a sink term to the bottom cell of the pumping well, situated at the center of the domain. Flow effects in the pumping well were achieved by setting a large anisotropy ratio in the local hydraulic conductivity between horizontal and vertical direction $\left(K_z/K_x = 10^5\right)$ in the pumping well central column.

[31] Finally, to simulate other Y fields, characterized by the same heterogeneous architecture but different variances, we multiplied each cell of the Y field by a factor of 2 and $2\sqrt{2}$ to obtain new synthetic fields with variances of $\sigma_Y^2 = 4$ and 8, respectively, for fields (A)–(C). No numerical convergence problems were found regardless the variance used.

2.2. Design of 3-D Transport Simulations and Estimation of Depth-Integrated BTCs

[32] We simulated conservative solute transport using the random-walk particle-tracking code RW3D [*Fernàndez-Garcia et al.*, 2005; *Salamon et al.*, 2006], which is efficiently coupled with Modflow-2000. In this algorithm, M is discretized into N_p particles (the mass of each particle being $m_p = M/N_p$). Based on the Langevin equation, each particle moves with a drift displacement, based on the radial flow velocities calculated at each cell of the domain by Modflow-2000, and a Brownian motion that accounts for local dispersive process. In our simulations, we set a constant porosity value of $\phi = 0.1$ in all simulations and $N_P = 3 \times 10^4$. Via a convergence test we found our results to not be sensitive to an additional number of particles.

[33] Injection wells were located at 16 different points in the domain around the extraction well as depicted in Figure 2. Each tracer test was independent of all others.

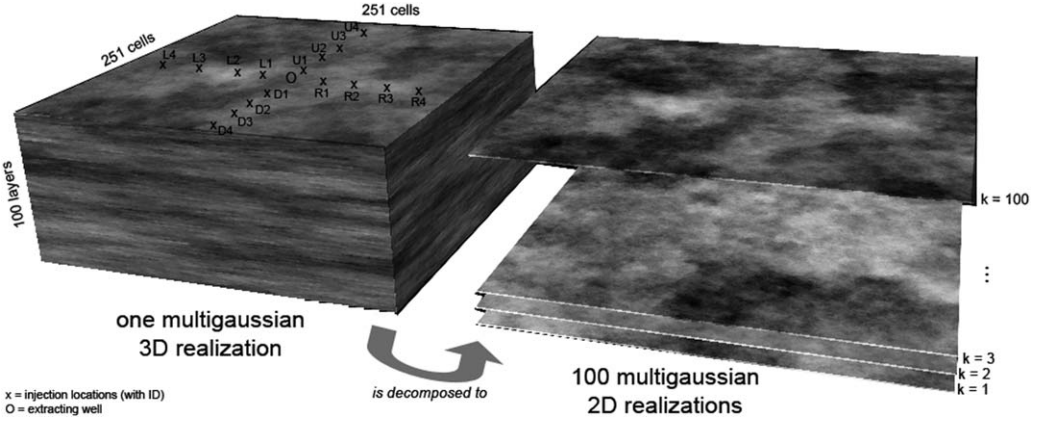

Figure 2. (left) The 3-D anisotropic field (B) used in the simulations, along with the position of the injection locations at various radial distances and angles around the well. (right) Schematic decomposition of a 3-D field into 100 layers, each of them representing a 2-D field with the same planar spatial correlation as the 3-D original counterpart.

The injection positions were oriented along the coordinate axes and were defined such that

[34] (1) injection boreholes at points U1, R1, L1, D1, located at $r = 5$ from the extraction well;

[35] (2) injection boreholes at points U2, R2, L2, D2, located at $r = 12$ 5 from the extraction well;

[36] (3) injection boreholes at points U3, R3, L3, D3, located at $r = 25$ from the extraction well; and

[37] (4) injection boreholes at points U4, R4, L4, D4, located at $r = 75$ from the extraction well.

[38] In all simulations, we started by setting an isotropic local dispersivity value of $\alpha = 0.25$, which ensures an $r/\alpha > 20$ at the injection locations. This was chosen considering $r/\alpha = 20$ as a suitable minimum value to ensure advection-dominated transport in radial flow problems in homogeneous aquifers [e.g., *Moench*, 1989]. We considered α to be isotropic in all directions (i.e., $\alpha_L = \alpha_T = \alpha_Z$, where L, T and Z indicate here the directions, respectively, collinear, transverse in the plane, and transverse in the vertical direction with the main flow direction), to avoid a possible bias in the interpretation of our results due to local anisotropic dispersive mechanisms.

[39] The number of particles in each layer was taken to be proportional to the local Darcy flux, to better represent flux-averaged conditions. Particles were introduced in the system from layer $k = 5$ to layer $k = 95$. Five cells were left empty at the top and at the bottom, to avoid rebounds and other uncontrolled boundary effects. Injection took place as a pulse, at the initial time ($t = 0$).

[40] We obtained "depth-integrated" BTCs after estimating the density of the distribution of travel times of the ensemble of released particles. As such, we did not keep track of where (at which depth) particles were injected. Since each particle carries the same amount of mass (m_p), the estimated density distribution of travel time was equivalent to the estimation of a normalized BTC.

[41] The estimation of the density function was based on the automatic optimal kernel density estimator algorithm described by *Fernàndez-Garcia and Sanchez Vila* [2011]. The numerical solution was successfully tested under homogeneous conditions against the analytical formulae of *Moench* [1989] and *Gelhar and Collins* [1971], to ensure that measured transport was not affected by boundary conditions.

2.3. An Illustrative Result of a Depth-Integrated BTC

[42] Let us first analyze some key aspects involved in the formation of a BTC obtained in one specific simulation. This is done to highlight the main phenomenological features needed to understand subsequent results. As our example, we considered injection at location L4 in field (B) (Figure 2) with $\sigma_Y^2 = 4$. Figure 3 is divided in four subplots, each of them representing the position of 1000 particles (above) and the "depth-integrated" BTCs (below) collected at the well at different times ranging from the initial injection time to a late time when the vast majority of particles have been captured at the well. The background colors represent the distribution of the (log) hydraulic conductivities on the vertical section parallel to the x axis, passing through both the injection and the extraction wells. Note that a consistent system of units was used throughout this work.

[43] At the initial time particles are concentrated in the highly conductive areas along the vertical section where Darcy velocities are higher (red pixels), while only a few particles are located in less conductive areas (green pixels).

[44] At the first earlier intermediate time, particles located initially within the higher Y zones have traveled greater distances, eventually reaching the extraction well, compared to those located in initially lower permeability areas. Since a large number of particles were initially injected in relatively high Y areas, the concentration peak appears at a relatively early time.

[45] At the second intermediate time, most of the particles (i.e., mass) have been collected, and only a few remain in the system. Note that the BTC scales very differently before and after this time. In particular, a fairly well-defined tail with behavior similar to $c \sim t^{-1}$ is clearly visible from this moment on.

[46] This example indicates that our numerical settings were able to produce anomalous transport which gives rise to heavy-tailed BTCs, similar to experimental observations. See, for example, Figure 3 as compared to case E1 case in Figure 1. We could therefore take advantage of the numerical model to see whether we could provide a physical explanation for $m \approx 1$. To address this issue in detail, which will be more thoroughly discussed in section 4, we studied the impact of imperfect stratification in the 3-D model.

2.4. Simulation of "Multilevel" Transport

[47] To evaluate the variability of solute mass arriving at different depths in a fully penetrating pumping well, we propose the following approach, which is graphically summarized in Figure 2. We noted that in radial convergent flow, planar flow is dominant with respect to vertical flow. Moreover, at relatively short injection distances compared with the horizontal integral scales, plumes in each planar layer migrate practically independently from those in other planar layers. This effect is enhanced in fields displaying axisymmetric anisotropy. Figure 3 illustrates this behavior, where it was found that particles move mainly horizontally.

[48] Noting that negligible vertical velocities and transverse dispersion lead to particle paths that follow primarily the horizontal plane in which particles are initially injected, we proceeded as follows. We separated each k layer making up the 3-D block and use them as independent 2-D Y fields. The new 2-D fields have 251 cells per side with unit thickness ($b = 1$). They have the same horizontal integral scales I_x, I_y but due to the effects of subsampling, (slightly) smaller variance than the original 3-D Y field (e.g., from $\sigma_Y^2 \approx 4$ in the 3-D simulations to an average value of $\sigma_Y^2 \approx 3.5$ for the 2-D simulations). We did not renormalized the variance in each layer to obtain the same original value as the 3-D simulation since our aim was to evaluate the effects of the stratified transport in each layer within the 3-D formation and asked how much information does one obtain from 2-D versus the full 3-D system?

[49] In each of the $N_k = 100$ layers, we calculated 2-D flow and transport and estimated BTCs, using the same procedure described in previous sections. We injected the same mass (M) per layer as a pulse release directly at the same 16 positions used for the 3-D simulations. In each layer, we imposed the same discharge rate as in the 3-D counterparts (Q). We thus obtained 100 BTCs (one for

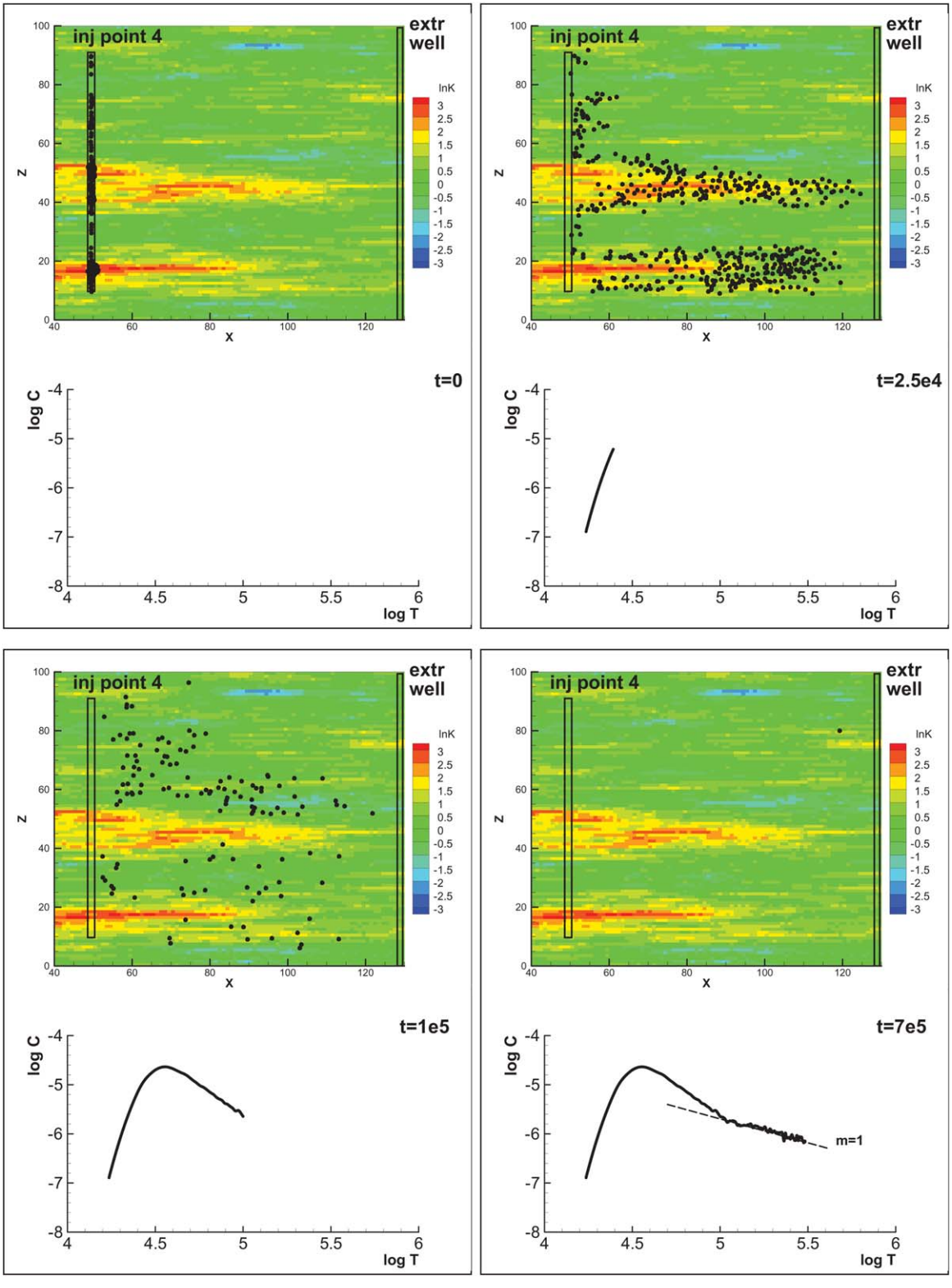

Figure 3. Particle displacement at different temporal steps during the simulation of a CFTT in the anisotropic field (B) with $\sigma_Y^2 = 4$, after injecting from position L4. (top) Particles are plotted along with the distribution of log-transformed hydraulic conductivities, Y, at the central section of the domain. (bottom) The evolution of the BTC estimated as "depth-integrated" particle mass density at the extraction well.

each layer) for each injection position; we call BTCs obtained from this approach "2-D BTCs."

[50] As an illustrative example, we considered again the injection taking place at location L4 in field (B) with $\sigma_Y^2 = 4$. In Figure 4 the "depth-integrated" BTC obtained from 3-D transport (Figure 3, bottom right) is depicted as a thick, black line. Along with that, the gray curves represent the 100 BTCs obtained after injecting in each layer making up the 3-D block (i.e., the 2-D BTCs). We note from Figure 4 that unlike the 3-D integrated case, 2-D BTCs never show heavy PL tailing but are mostly symmetric. This means that the behavior of most of these BTCs is much more similar to that of a homogeneous Y field rather than the typical curves in heterogeneous media. Moreover, 2-D BTCs look like "convolved" versions of one another, as indicated by the spread of the maximum peak of concentrations on each BTC (marked by a blue square). This behavior is qualitatively very similar to the one found by *Becker and Shapiro* [2003], where they reproduced depth-integrated BTCs as a convolution of independent BTC obtained from transport in individual channels. We discuss and compare their results with ours in section 4.

[51] The difference between the estimated concentration for 2-D and 3-D BTCs is due to the fact that in 2-D realizations the injected mass is equal to the total injected mass for the 3-D cases, while in each layer of the 3-D simulations mass enters as a flux-weighted amount. In addition, to compare different BTCs, we need to express variables in terms of dimensionless parameters. To this end we used the following dimensionless quantities:

[52] (1) A estimated mass density, $\hat{p}(t,k)$, was obtained by

$$\hat{p}(t,k) = \frac{1}{D_F(k)} \frac{QC(t)}{\int QC(t)\mathrm{d}t} \tag{1}$$

where D_F is a dilution factor that is proportional to the mass injected in the system at each layer in 2-D simulations and the 3-D simulations. The parameter $C(t)$ is the resident concentration at the well locations, and D_F can be defined as

$$D_F(k) = \frac{q_x(k)}{\sum_{k=1}^{N_L} q_x(k)} \tag{2}$$

where $q_x(k)$ is the local seepage velocity at each injection location.

[53] (2) A normalized time (t_c) was defined such that

$$t_c = \frac{t}{t_{adv}} \tag{3}$$

where t_{adv} is the advection time [e.g., *Moench*, 1989], such that

$$t_{adv} = \frac{\pi r^2 b \phi}{Q} \tag{4}$$

where b is the aquifer thickness ($b = 1$ for 2-D simulations and $b = 100$ for 3-D simulations). This normalization ensures that the concentration peaks of the BTCs under CFTTs performed from injection locations at different distances (r) from the pumping well always collapse around $t_c = 1$ for homogeneous aquifers.

[54] (3) A normalized injection distance (r_λ) was obtained to compare BTCs obtained from different realizations with different integral scales. We normalized r by the horizontal integral scale of each field, I_x, such that

$$r_\lambda = \frac{r}{I_x} \tag{5}$$

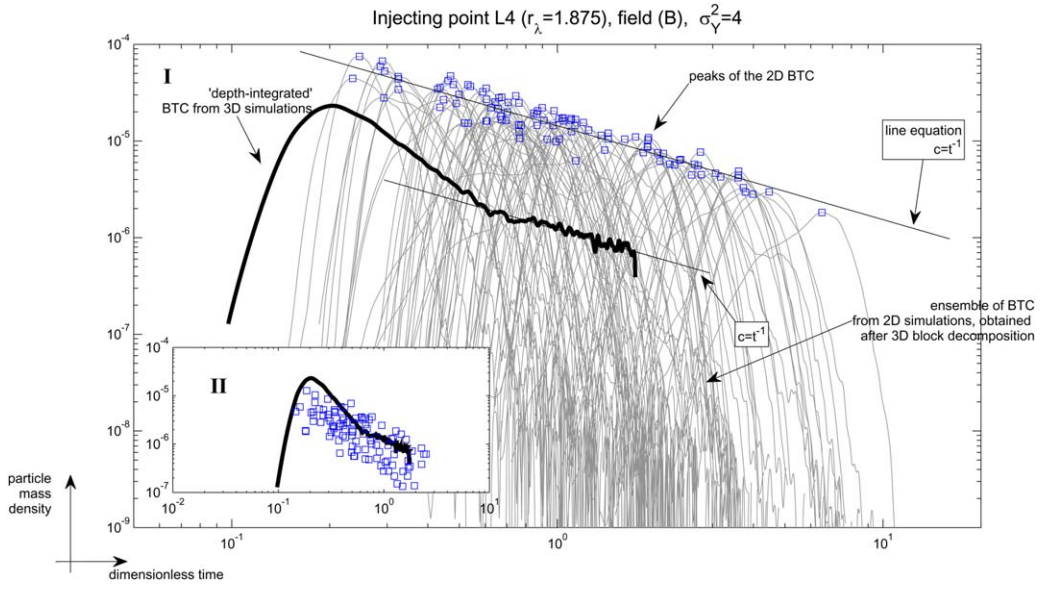

Figure 4. Superposition of particles' probability density functions (BTC) obtained after injecting at L4 in the anisotropic field (B) with $\sigma_Y^2 = 4$ and $r_\lambda = 1.875$. The 3-D BTC is plotted with a dark strong line. The 2-D BTC from "layer injection" is plotted with gray colors. A red 2-D curve is plotted to emphasize one of the rare examples of heavy-tailed 2-D BTC. The peaks of the 2-D are marked in blue. Two lines with slope $c \sim t^{-1}$ are overlapping the 2-D peak cloud and the late time of the 3-D BTCs to highlight this late-time scaling behavior.

[55] (4) A normalized vertical injection length (L_z) was obtained to measure "how stratified" the solute is injected into the system, and thus how homogenized the solute transport is for short travel distances. The parameter L_z was found as the ratio between the aquifer thickness (b, which also corresponds to the particle injection length) and the vertical integral scale I_z, such as

$$L_z = \frac{b}{I_z} \tag{6}$$

[56] Note that in equation (4), we used r rather than r_λ since we wanted to emphasize the effect of heterogeneity on the solute travel time.

[57] Let us first analyze the case when D_F was not accounted for and the same mass was injected in each 2-D simulation and equal to the one imposed for the 3-D simulations (M). This is plotted in Figure 4I (big window) from which we can infer two fundamental issues. First, it looks like 2-D settings that are not suitable to reproduce anomalous transport, even though the 2-D simulations were performed with similar horizontal variogram statistics (e.g., same correlation lengths but slightly smaller variance) as the 3-D counterparts. We believe this is due to the use of unconditional 2-D SGS simulations, a result that is similar to what was observed by *Willmann et al*. [2008]. Second, the ensemble of peak concentrations for the 2-D BTCs (indicated by squares in Figure 4) scales like a PL with unit slope, i.e., of the form $\hat{p}(t) \sim t_c^{-1}$.

[58] We also observe the effect of rescaling particle density with D_F. This is plotted in Figure 4II (small window), where to avoid redundancy we only plot the 2-D BTC peaks. It can be seen that the concentration peaks were found at similar concentrations to the 3-D counterparts. This confirms that the mass distribution among layers can perhaps be thought of as a convolution of effects giving rise to such tailing (i.e., as in *Becker and Shapiro* [2003]). There is not an exact match between the 2-D peaks and 3-D curves (as it would be expected, for instance, analyzing multilevel concentrations at the well) due to intrinsically different flow structures of the 2-D and 3-D flow simulations.

[59] In the next section, we present the most relevant findings extracted from the additional simulations, in order to find the impact of the degree of heterogeneity on the different late-time slopes of the BTCs.

3. Comparison of Different Cases

[60] Here we describe other significant results of our numerical analysis, which we compared with the illustrative example in Figure 4. The goal was to show how exportable the scaling $\hat{p}(t) \sim t_c^{-1}$ of the depth-integrated BTC tailing at late times is. We also aimed to link this slope to some characteristic physical patterns to gain a proper physical understanding of why and when it occurs.

3.1. Evaluation of the Anisotropic Case (Field (B)) With $\sigma_Y^2 = 4$

[61] In this part, we compare the results for other injection locations within the anisotropic field (B) with $\sigma_Y^2 = 4$. For this field the normalized injection length was $L_z = 25$.

[62] In addition to the injection at L4, in Figure 5 we plot the results for three other injection locations,

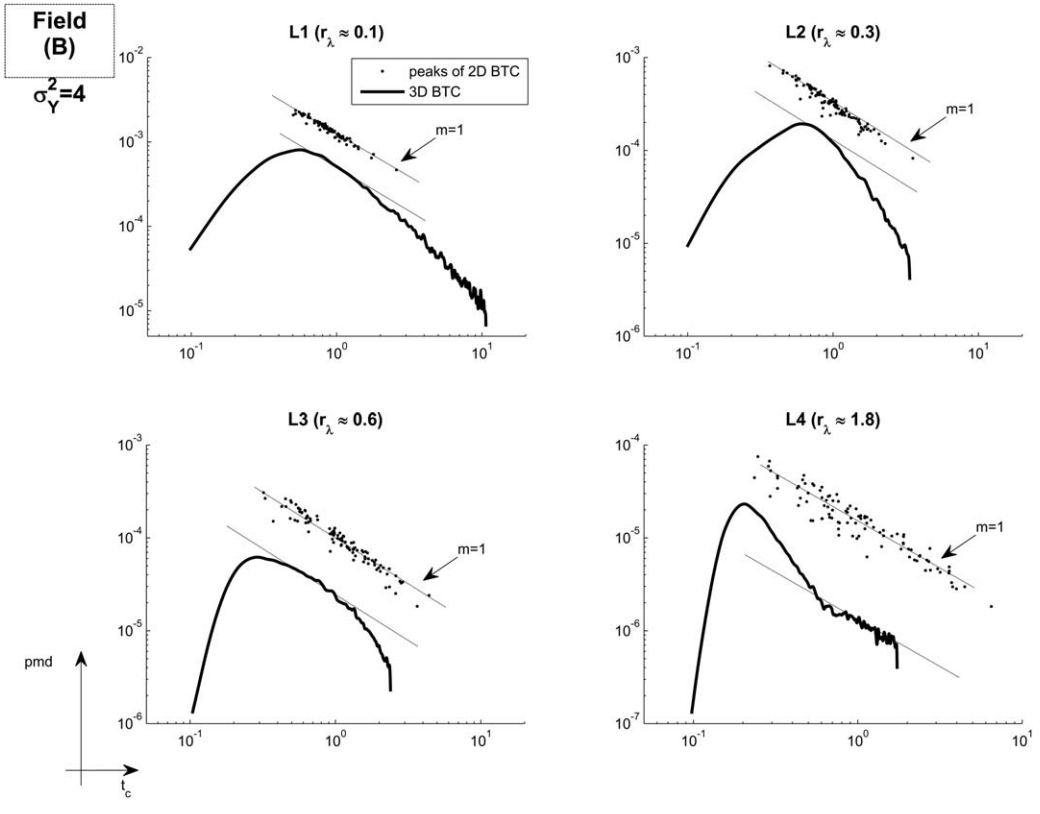

Figure 5. The 3-D BTCs (and relative peak distributions) obtained after injecting in the anisotropy field (B) with $\sigma_Y^2 = 4$, at L points. Notice that the behavior $\hat{p}(t) \sim t_c^{-1}$ can be fitted only at L4 ($r_\lambda \approx 1.8$), while the other locations display a more symmetric behavior.

specifically at L1, L2, and L3. These cases look at injections at different distances from the pumping well. In Figure 5, the depth-integrated BTCs (black line) are reported along with a cloud of points representing the peaks of the 2-D BTC simulations, which were obtained using the "layer decomposition" approach described above.

[63] We observe that the depth-integrated BTCs always show some form of heavy-tailed distribution, but that the BTC slopes change as the injection location r_λ increases. Specifically, we observe that injections at short distances (L1 and L2) where the normalized injection distance is small $(r_\lambda \approx 0.1, 0.3)$, tailing is observed with constant slope, but different from (faster than) $\hat{p}(t) \sim t_c^{-1}$. This regime is on the other hand clearly observed at the largest injection distance (L4), where $r_\lambda \approx 1.8$. A subtle look at the data suggests that a regime qualitatively like $\hat{p}(t) \sim t_c^{-1}$ may exist to some extent in all cases but persists for much longer times as the injection distance approaches $r_\lambda \approx 1.8$.

[64] Looking at the "cloud" of 2-D peaks, it seems that they align well with $\hat{p}(t) \sim t_c^{-1}$ for all injection locations. However, it is visually evident that the relative spread of these point varies, being narrowest at L1 and widest at L4, with L2 and L3 as intermediate cases. To quantify this spread, we calculated the spread of this "cloud," defining

$$\sigma_t^2 = \frac{1}{N_k - 1} \sum_{k=1}^{N_k} \left(\left| \log\left(t_{pk}(k)\right) - \overline{\log\left(t_{pk}\right)} \right| \right) \tag{7}$$

where $\log\left(t_{pk}\right)$ represents the base 10 log-transformed value of the dimensionless time coordinate at which the peaks are observed. The parameter $\log\left(t_{pk}\right)$ is the average of log-transformed dimensionless peak times over the N_k layers. A low value for this spread (e.g., $\sigma_t^2 \to 0$) would indicate that transport is very similar in all the horizons (e.g., relatively homogeneous medium), while large variances represent stronger heterogeneity induced spreading.

[65] For injection location L1, $\sigma_t^2 = 0.076$. This low value is due to the relatively short injection distance, which prevents the tracer from displaying strong vertical stratification of the concentration measurable in terms of "depth-integrated" BTCs. At L2 and L3, $\sigma_t^2 = 0.165$ and 0.324, respectively, emphasizing the development of vertical stratification of the plume, and enhanced differences between layers. At L4, where r_λ is close to the horizontal integral scale, $\sigma_t^2 = 0.561$, indicating that the plume is more stratified than in the other cases and is heavily controlled by the different properties of each layer.

[66] Note two fundamental points. Anomalous tailing like $\hat{p}(t) \sim t_c^{-1}$ clearly takes place (1) when the solute travel distance is of the order of the horizontal heterogeneous scale of the multi-Gaussian field (i.e., R of the order of I_X) and (2) when σ_t^2 is maximum among the four injection points L1–L4. As shown in the following sections, these characteristic patterns will be also found for the other field geometries and variances.

3.2. Comparison With Isotropic Fields

[67] Noting that field (B) (Figure 2) has an anisotropic correlated structure of hydraulic conductivity, a reasonable question is whether the stratification of the plume is controlled dominantly by the stratified distribution of Y. We therefore evaluated the behavior of BTCs for the 2-D and 3-D Y fields associated with fields (A) and (C), which are isotropic.

[68] The curves for field (A) are plotted in Figure 6. For this case, the normalized injection distance is again the same as for field (B), i.e., $L_z = 25$. We plot only the curves corresponding to injection wells R1–R4 since the other arrays (L, U, D) display similar behavior. As $I_x = 4$ in this field, the normalized injection distance is close to unity for R1 $(r_\lambda \approx 1.8)$ and increases up to $r_\lambda \approx 18$ for R4. At position R1, 3-D BTCs display anomalous tailing with a behavior very similar to $\hat{p}(t) \sim t^{-1}$ right after its peak. As soon as the injection distance increases, this behavior seems to diminish, until it is no longer truly observable at R4.

[69] Observing the peak distribution, the spread at R1 is larger $\left(\sigma_t^2 = 0.621\right)$ than at R2 and R3 $\left(\sigma_t^2 = 0.372\right)$. At R4, since no tailing develops, one expects σ_t^2 to be the smallest value; however, it is slightly higher than for the other cases (0.717). It should be noted from Figure 6 that this latter value can be biased by the presence of a few outliers (a few layers displaying very large peak time). Disregarding the five largest values at peak times (5% of the total number of layers) leads σ_t^2 to reduce to 0.341, which is smaller than for R1, R2, and R3.

[70] The curves for field (C) are plotted in Figure 7. In this case, $L_z = 2.5$, which means more homogenization in the BTCs might be expected. We find that at very short normalized injection distances, such as R1 $(r_\lambda = 0.1)$, no heavy-tailed behavior is clearly observed in the 3-D BTC, while a tailing behavior emerges once again as the normalized injection distance increases to order one and a broad time range of peak arrival times occurs: e.g., at R4 $(r_\lambda = 1.8)$, BTC scales as $\hat{p}(t) \sim t_c^{-1}$. Again, field (C) displays a similar behavior as in the other fields (A) and (B). The distribution of 2-D peaks is very narrow when no tailing develops (at R1, $\sigma_t^2 = 0.07$), and it is the largest among the four injection location at R4 $\left(\sigma_t^2 = 0.25\right)$.

[71] We found in BTCs from fields (A) and (C) a similar behavior as the one found on BTCs for field (B). Accounting for the 2-D peak outliers' values at R4 in field (A), the new observations suggest again that $\hat{p}(t) \sim t_c^{-1}$ is observed in the 3-D BTC when σ_t^2 is the largest among the four injection point in each field and $r_\lambda \approx 1$ is met.

[72] The similar behavior between BTCs from the isotropic fields (A) and (C) and BTCs from stratified field (B) can be explained considering the initial vertical stratification of the tracer, which is quite relevant and independent of the statistical structure of the media in our single realization analysis. It seems that if the solute travel distance is very small compared with the injection distance, the system acts as practically homogeneous and solutes tend to arrive at similar times, while if the solute travel distance is very large, transport becomes more homogenized, as the solute samples a sufficient number of heterogeneous scales before being collected at the well.

3.3. Effect of Changing the Injection Location

[73] In single stochastic realizations and particularly under radial flow conditions, solute behavior is hardly ergodic. Nonergodicity of the plume means that BTCs can vary drastically from realization to realization. A direct consequence of ergodicity would be that all curves would

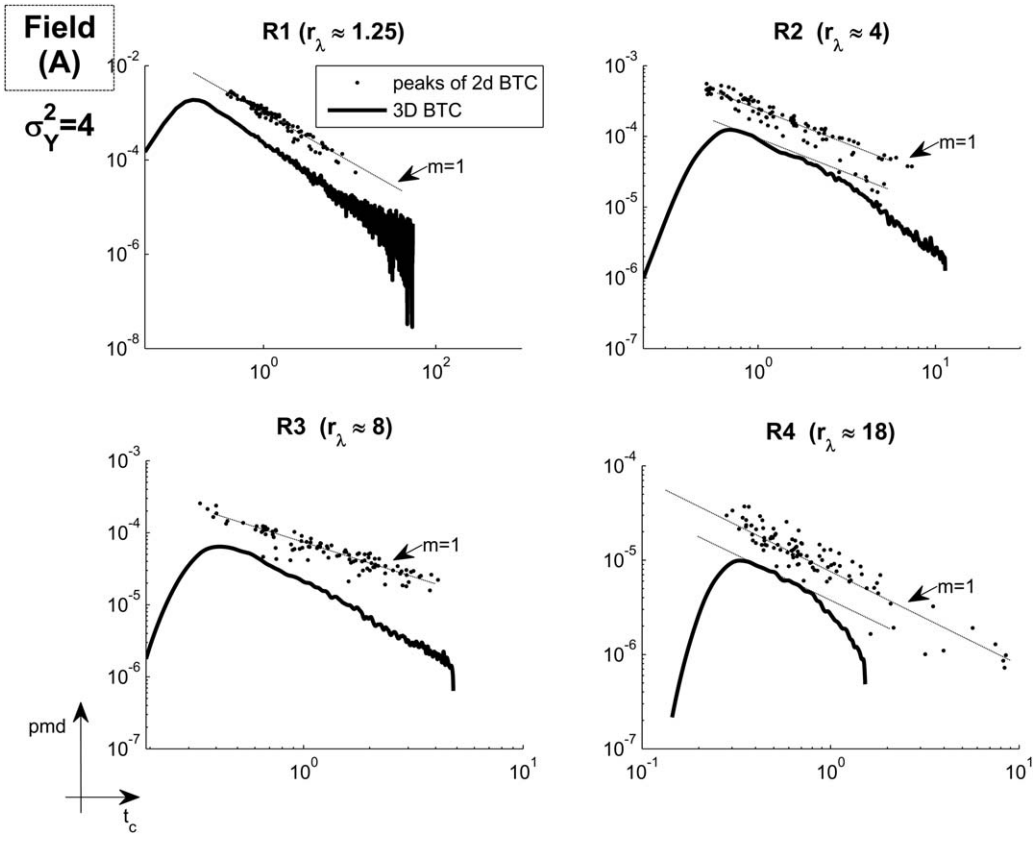

Figure 6. The 3-D BTCs (and relative peak distributions) obtained after injecting in the isotropic field (A) with $\sigma_Y^2 = 4$, at R points. Notice that the behavior $\hat{p}(t) \sim t_c^{-1}$ is very similar to the 3-D BTC slope at L1 $(r_\lambda \approx 1.25)$ but tends to diverge as long as the injection distance increases. At R4, the BTCs are more symmetric.

not depend on the specific injection location, but only on its distance to the well. In our realizations, this is clearly not the case, and so we compared solutions obtained for the BTCs recorded at points located at the same injection distance from different directions.

[74] Referring to Figure 2 for the position map, we plot in Figure 8 the depth-integrated BTCs and relative 2-D peaks obtained for locations D2, L2, D4, and L4 for all three fields (A)–(C). For these simulations, we kept $\sigma_Y^2 = 4$.

[75] For field (A), we observe that the shapes of the BTCs are slightly different for injection locations L2 and D2 $(r_\lambda \approx 3)$, and no PL tail is observed. At L4 $(r_\lambda \approx 18)$, BTCs show a well-defined $\hat{p}(t) \sim t_c^{-1}$ at late times; here the spread of the distribution of 2-D peaks is close to the unity (σ_t^2 at L4 = 0.701). At D4, the variance is slightly smaller than in the previous case $\left(\sigma_t^2 = 0.533\right)$, and analogously to what is seen for R4 (Figure 6), the BTC does not scale with $\hat{p}(t) \sim t_c^{-1}$ (see Figure 6).

[76] Looking now at the results from field (B), the late-time behavior of BTCs at D2 and L2 $(r_\lambda \approx 0.6)$ is practically the same, showing no constant PL tailing. Here the spread of the distribution of 2-D peaks is narrow ($\sigma_t^2 = 0.263$ for D2 and $\sigma_t^2 = 0.165$ for L2), indicating that once again the BTC does not develop for low vertical variability of the plume behavior. A more pronounced PL effect is found at D4, but not in the case of injection from L4. Again, despite the fact that both injection points are located at $r_\lambda \approx 1.8$, the spread of the 2-D peaks distribution is much higher for D4 $\left(\sigma_t^2 = 1.007\right)$ than at L4 $\left(\sigma_t^2 = 0.562\right)$.

[77] In field (C) (right), for injection locations D2 and L2 and L4, BTCs are found to follow a relatively similar symmetric behavior at late time. Only at D4 the BTC shows a more nonsymmetric distribution (roughly following $\hat{p}(t) \sim t_c^{-1}$, despite the presence of multiple peaks) Once again, the spread of the peaks is higher when BTCs display less symmetric distributions and more tailing ($\sigma_t^2 = 0.252$ at D4) than where no tailing occurs ($\sigma_t^2 = 0.045$ at D2; $\sigma_t^2 = 0.036$ at L2; $\sigma_t^2 = 0.056$ at L4).

[78] These results serve to highlight and confirm the previous hypothesis, i.e., that a combination of high σ_t^2 and r_λ close to unity to determine $\hat{p}(t) \sim t_c^{-1}$, independent of injection location and type of geological setting. It should be noticed that the characteristic values of σ_t^2 for tailing to develop vary from field to field. It is difficult at this level to build a general rule, if it exists, to quantitatively evaluate what this value should be for $\hat{p}(t) \sim t_c^{-1}$ to develop. For this purpose, additional numerical outcomes were needed. We address such an evaluation in the last section.

3.4. Effect of *Y* Variance

[79] We explore here the effect of the variance of the log-transformed hydraulic conductivity, σ_Y^2, on the BTC

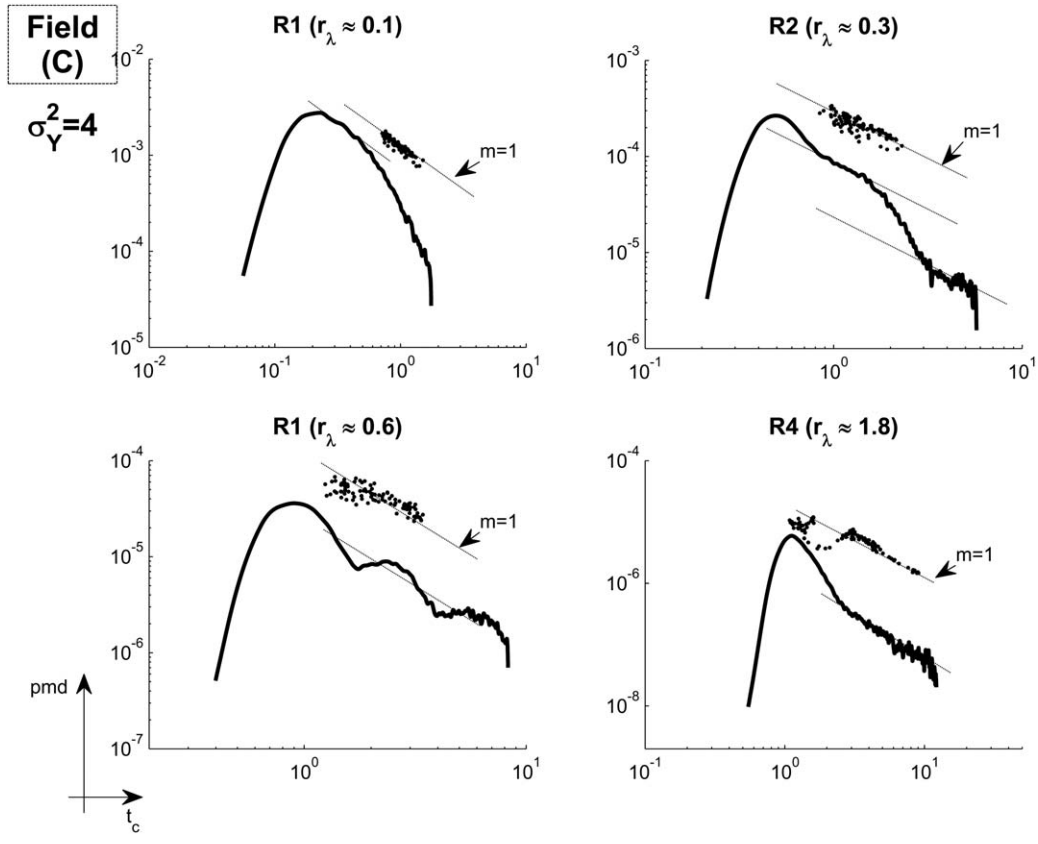

Figure 7. The 3-D BTCs (and relative peak distributions) obtained after injecting in the anisotropy field (C) with $\sigma_Y^2 = 4$, at R points. Notice that the behavior $\hat{p}(t) \sim t_c^{-1}$ can be fitted at L4 ($r_\lambda \approx 1.8$). From R1 to R4, the 3-D BTCs increasingly tend to heavy-tailed distributions; at R2 and R3, a PL behavior with $m = 1$ can be inferred at different intermediate portions of the BTCs.

tailing. In our analysis, we focused on values of $\sigma_Y^2 = 1, 4$, and 8. For illustrative purposes, we will use the example of anisotropic field (B) (Figure 2b), with injections from two different locations (L2 and L4). Again, these are chosen to illustrate results, and it is important to note that similar behavior was observed and conclusions made with observations from the other fields and locations. The results are displayed in Figure 9.

[80] As one might intuitively expect, the general effect of increasing σ_Y^2 is to increase σ_t^2. At L2, we observe that the variance of the 2-D peaks increases from $\sigma_t^2 = 0.038$ for $\sigma_Y^2 = 1$ to $\sigma_t^2 = 0.329$ for $\sigma_Y^2 = 8$. In none of the BTCs do we observe $\hat{p}(t) \sim t_c^{-1}$, which we attribute to the fact that injections take place very close to the well, and our hypothesized condition r_λ close to unity is not met.

[81] At L4 (where $r_\lambda \approx 1.8$), BTCs are more anomalous. While for $\sigma_Y^2 = 1$, with $\sigma_t^2 = 0.143$, BTCs do not show a clear PL behavior, this is much more visible for the larger variance cases of $\sigma_Y^2 = 4$ and 8, where $\hat{p}(t) \sim t_c^{-1}$ at the late time. In the two latter cases, σ_t^2 is 0.562 and 1.101, respectively.

[82] From this last analysis, we observe that the variance of log conductivity is a key controlling factor in the development of PL tailing on our BTCs. In particular though, these results provide evidence confirming our two other hypothesized conditions for $\hat{p}(t) \sim t_c^{-1}$, which are (1) an injection distance close to the integral scale and (2) a large spread of the 2-D peaks.

4. Discussion

[83] From our results, we observed so far that in many cases that meet certain conditions, a PL behavior of the form $\hat{p}(t) \sim t_c^{-1}$ develops on depth-integrated BTCs when collected during CFTTs in advection-dominated aquifers. This behavior is highly variable, but we identify common patterns to phenomenologically explain this behavior. In particular, we note that for $\hat{p}(t) \sim t_c^{-1}$ to take place on BTCs, the normalized injection distances should be $r_\lambda \approx 1$. If it is much smaller or much larger than this it will not occur, although BTCs may still be highly nonsymmetric. Once this condition is met, the PL extends over larger time ranges with increasing σ_Y^2, or better said larger σ_t^2, which is controlled by σ_Y^2. Peak times have been already reported in the literature to characterize flow and transport variables [e.g., *Bellin and Rubin*, 2004]; here we can attribute a large σ_t^2 to large variability of point-to-point connectivity patterns [e.g., *Trinchero et al.*, 2008] along the vertical injection line.

[84] We note that the presented findings are based on a finite set of realizations, and caution should be taken in trying to generalize them. However, based on our observations, there are some questions we would like to address here: (1) Is there, and if so, how strong is the correlation between 2-D peak spreading and 3-D tailing in our simulations? (2) Does local dispersivity play a key role in 3-D tailing and/or 2-D peak spreading? (3) Can we explain

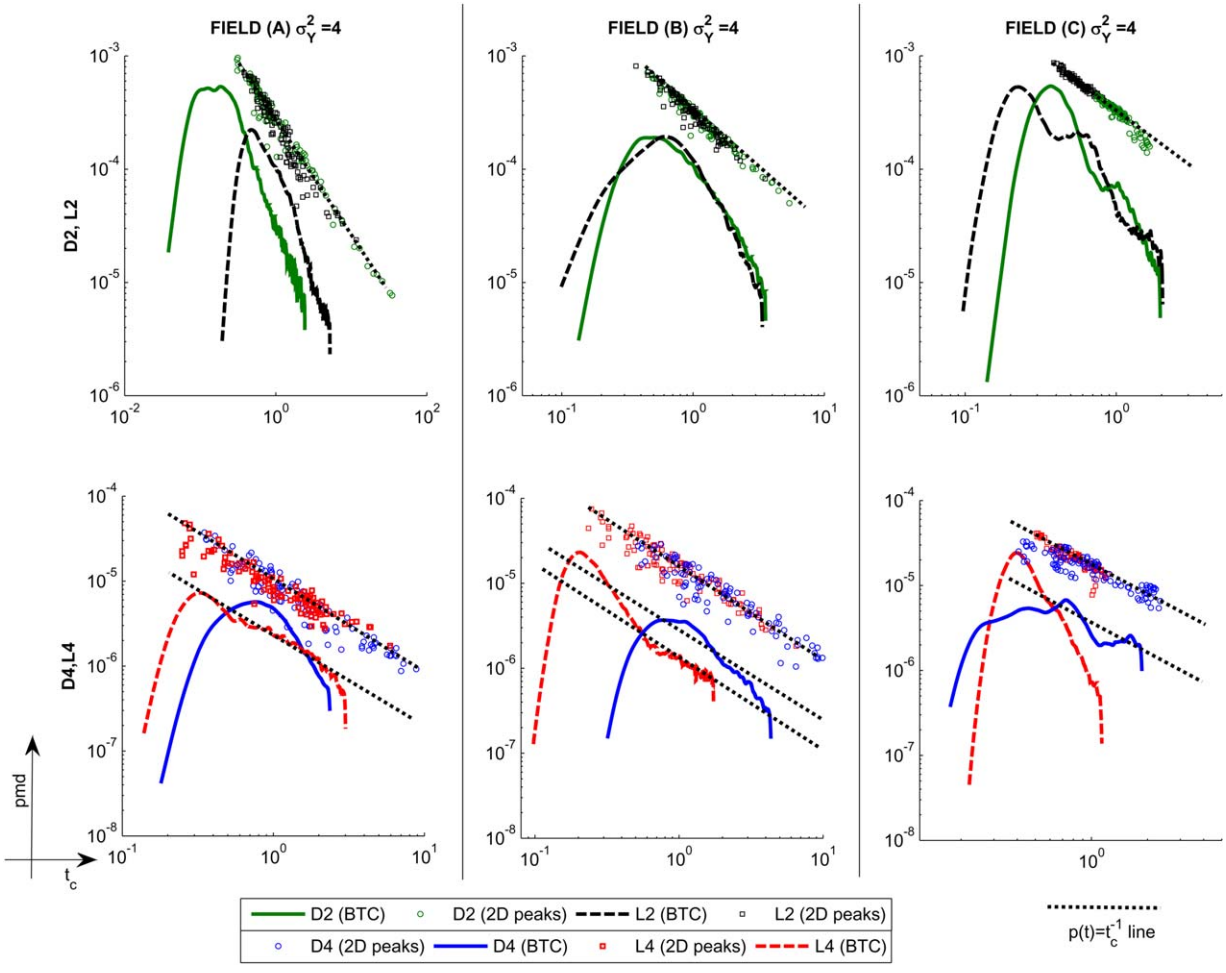

Figure 8. The 3-D BTCs (and relative peak distributions) after injecting in the three fields A, B, and C with $\sigma_Y^2 = 4$, at different locations. The line indicates which BTCs display a behavior like $\hat{p}(t) \sim t_c^{-1}$.

tailing a with unit slope on both 2-D peak distributions and in late-time 3-D BTCs? We provide answers in the following.

4.1. Can Peak Spreading and Tailing Be Related?

[85] We observe that the peak spreading, measured by σ_t^2, has to surpass some critical threshold for the behavior $\hat{p}(t) \sim t_c^{-1}$ on the BTC to occur, but so far we have only qualitatively indicated that σ_t^2 has to be generally "large" for this regime to take place. It would be useful to find a more quantitative relationship between this value and some parameters it may depend on.

[86] We started to compare if peak spreading can be related with the nonsymmetric degree of the 3-D BTCs. Tailing has been seen to be highly variable from case to case, and peak distribution is in addition nonunique between different types of fields. Let us focus one moment only on those injection locations providing conditions for the 3-D BTCs to display $\hat{p}(t) \sim t_c^{-1}$. As indicated in section 3.2, this condition takes place for field (A) at R1, where $\sigma_t^2 = 0.621$, for field (B) at L4, where $\sigma_t^2 = 0.561$, and for field (C) at R4, where $\sigma_t^2 = 0.25$. Note that a value of $\sigma_t^2 = 0.25$, which is sufficient for field (C) to generate $\hat{p}(t) \sim t_c^{-1}$, is not sufficient for field (B), as in the latter field it would correspond to an intermediate injection point between L2 and L3, which do not show such a well-defined PL behavior. However, L2 and L3 still display anomalous behavior.

[87] We explore here, for each field (A)–(C) and for all the system variances $\left(\sigma_Y^2 = 1, 4, 8\right)$, whether a relationship can be built between peak spreading and the nonsymmetric behavior of 3-D BTCs at least for those injection points that satisfy the $r_\lambda \approx 1$. We plot in Figure 10, for each of these points, the corresponding peak spreading distance $\left(\sigma_t^2\right)$ and another characteristic distance (β) indicating the degree of tailing of the corresponding 3-D BTC. The latter was calculated as the normalized distance between the peak concentration time of the 3-D BTC (t_{pk}) and the first moment of the travel time distribution $(\bar{t})$ such that

$$\beta = \frac{t_{pk} - \bar{t}}{\bar{t}} \tag{8}$$

[88] Note that a value of $\beta \to 0$ indicates that the peak time corresponds to the center of mass of the distribution, which means a symmetric distribution, similar, for instance, to the BTC modeled under homogeneous conditions.

[89] Results are shown in Figure 10. In field (A) the points that satisfy the required condition $r_\lambda \approx 1$ correspond to injection locations R1, U1, D1, and L1. For fields (B)

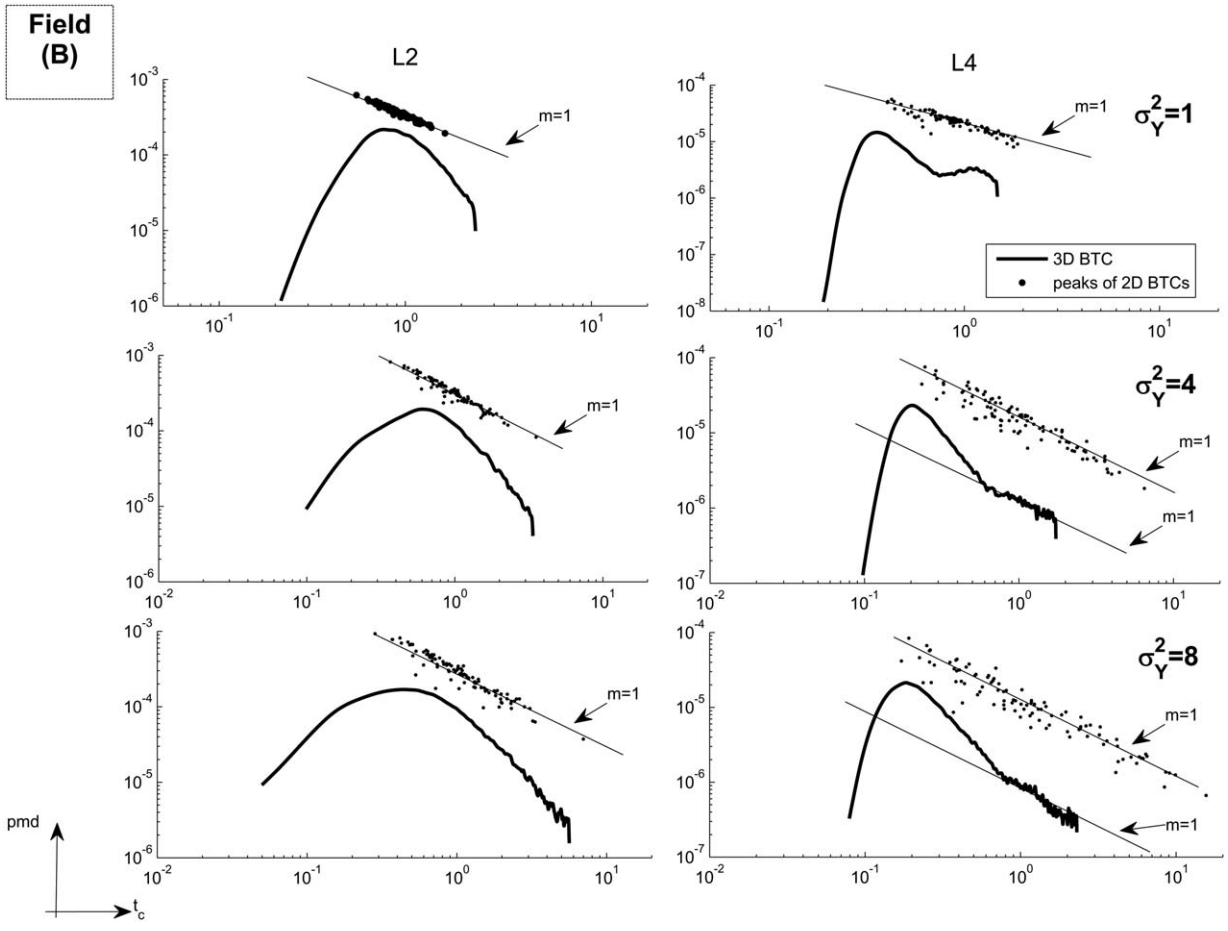

Figure 9. The 3-D BTCs (and relative peak distributions) for the anisotropic field (B) for variable variance ($\sigma_Y^2 = 1, 4, 8$, respectively, from the top to the bottom of the plot), at two injection locations, L2 and L4. Note that BTC tends to scale as a PL with $m \approx 1$ for L4 in case of variance $\sigma_Y^2 = 4$ and 8, which also show distribution of 2-D peaks more spread than in the case where m is not found close to the unit.

and (C), on the other hand, these injection locations are R4, U4, D4, and L4. In Figure 10 it can be seen that there is a good correlation between σ_t^2 and β, but there is a striking difference between the behavior of points in field (A) (using the local dispersivity value of $\alpha = 0.25$) and the ones in fields (B) and (C). In the first case, points at (A) with $\alpha = 0.25$ are distributed very similarly to a PL function of the form $\sigma_t^2 \propto \beta^{0.5}$. For the other case, if we exclude some outliers (such as the point indicated by "N") in the plot, points (B) and (C) seem to be still PL distributed, but this time of the form $\sigma_t^2 \propto \beta^2$. This result reveals several important aspects.

[90] (1) We observe that for field (A) with $\alpha = 0.25$, a short increase of the 2-D peak variance (i.e., higher independent behavior of strata in the domain) leads to higher tailing, while this regime is much slower for fields (B) and (C) (i.e., more variability between strata is needed on fields (B) and (C) to generate the same amount of nonsymmetric behavior as in the field (A)).

[91] (2) The plot suggests that the behavior for fields (B) and (C) is very similar, despite the characteristic vertical injection distance L_z being an order of magnitude larger in field (B) than in field (C). This means that in this configuration, solute initial stratification due to the flux-weighted injection mode dominates, on single realizations, over the statistical distribution of Y.

[92] (3) The plot quantitatively suggests how total variance $c_{pk} = \frac{M}{2Qt_{pk}}\left(\frac{4}{3}\pi\frac{a_L}{r}\right)$ controls the distribution of peak time $\left(\sigma_t^2\right)$ and in turn the nonsymmetric degree of the 3-D BTC (β). As one might expect, this figure intuitively suggests that the larger the total variance in 3-D simulations, the larger the difference in connectivity displayed by the different layers of the formation, and the larger the effect of stratification.

4.2. Are Results Sensitive to the Local Dispersivity?

[93] All simulations presented so far have an isotropic local dispersivity $\alpha = 0.25$. This value was set to enforce that dimensionless parameter $r/\alpha > 20$ and maintain advection-dominated transport. Another similar important dimensionless parameter that might play an important role is

$$I_\alpha = \frac{I}{\alpha} \tag{9}$$

which can be thought of as a Peclet number. Typically, large I_α suggests advection-dominated transport, while low

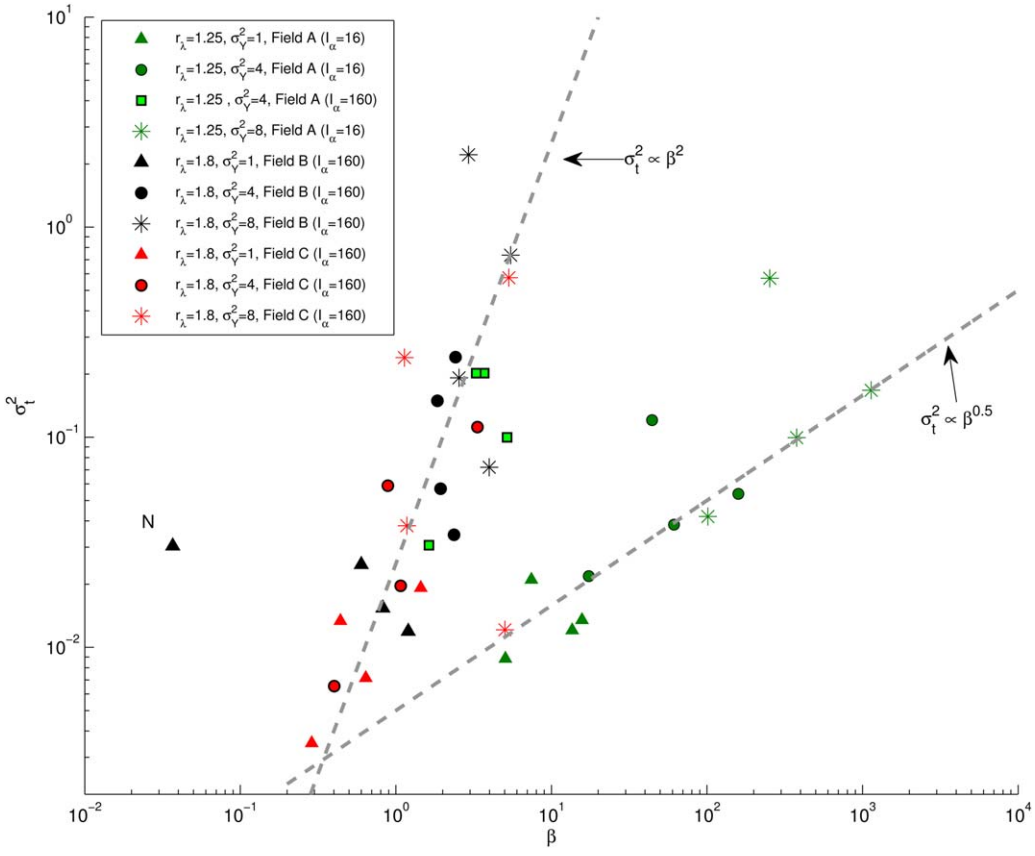

Figure 10. Relationship between 2-D peak spreading, σ_Y^2, and degree of tailing of 3-D BTCs, β, measured for fields (A)–(C) using normalized injection distance $r_\lambda \approx 1$ and different variances σ_Y^2. We note that all the points having $I_\alpha = 160$ are collinear with a PL correlation with a slope of 2, while points having $I_\alpha = 16$ are collinear with a PL correlation with a slope of 0.5.

values represent dispersion-dominated regimes. In our simulations, fields (B) and (C) have $I_\alpha = 160$ (considering $I = I_x$ in field (B)), while field (A) only has $I_\alpha = 16$. Note that the two correlations empirically suggested in Figure 10 discriminate field (A) with fields (B) and (C), which may suggest this is a reflection of different I_α values.

[94] To explore this point, we repeated the simulations for the field (A), with $\alpha = 0.025$, which sets $I_\alpha = 160$, the same for the field (B) and (C) simulations. For brevity, we focus only on the results with variance of $\sigma_Y^2 = 4$, although all other cases were considered also. Figure 10 also includes the results of σ_t^2 against β from these simulations (green squares). These points behave much like those of fields (B) and (C), i.e., a regime close to $\sigma_t^2 \propto \beta^2$. Figure 11 compares the original BTCs and peak distributions to the new ones (in red).

[95] The results indicate that local dispersivity plays an important role in the distribution of arrival times, but not on the phenomenon relating to BTC slope:

[96] (1) Figure 10 suggests that a reduction of α yields a reduction in β (the BTCs tend to have less persistent tailing and thus asymmetry), while the 2-D peak spread varies quite little. This can be seen in Figure 11, where the red ($I_\alpha = 160$) BTCs are narrower than their black ($I_\alpha = 16$) counterparts, while the dots reflecting the 2-D peaks display qualitatively similar scatter. This behavior indicates that the effects of transverse dispersivity may not be negligible for the development of anomalous behavior in radially convergent transport in 3-D systems.

[97] (2) From Figure 11 we note that tailing occurs over a narrower range of times, but it does seem that the tail slope is not strongly influenced by α; this means that likely, the slope is more controlled by stratification and connectivity rather than by local dispersion, and transverse dispersivity may not be negligible for the development of PL-like slopes on BTCs. For R1, the qualitative behavior $\hat{p}(t) \sim t_c^{-1}$ at later times is still somewhat visible in the new BTC with low α (red curve), even if the "length" of this tail is much shorter than for the simulation with a larger α. Discrepancies between the BTCs diminish as the normalized injection distances increase suggesting less sensitivity to local dispersivity values, probably due to comparable heterogeneity sampling by the particles over very large times.

4.3. What Does $\hat{p}(t) \sim t^{-1}$ Scaling Mean?

[98] To explain why the specific PL behavior with $m = 1$ arises on depth-integrated BTCs, let us first consider why this occur on the slope of the peaks of 2-D BTCs. We already noticed from Figure 3 that the architecture of the tracer, once it has been injected into the well, is stratified, due to the flux-weighted scheme. Such stratification is due to the existence of hydraulic heterogeneities that condition (a) the mass injected in each layer, which depends exclusively on the flow velocities at the cells located along the

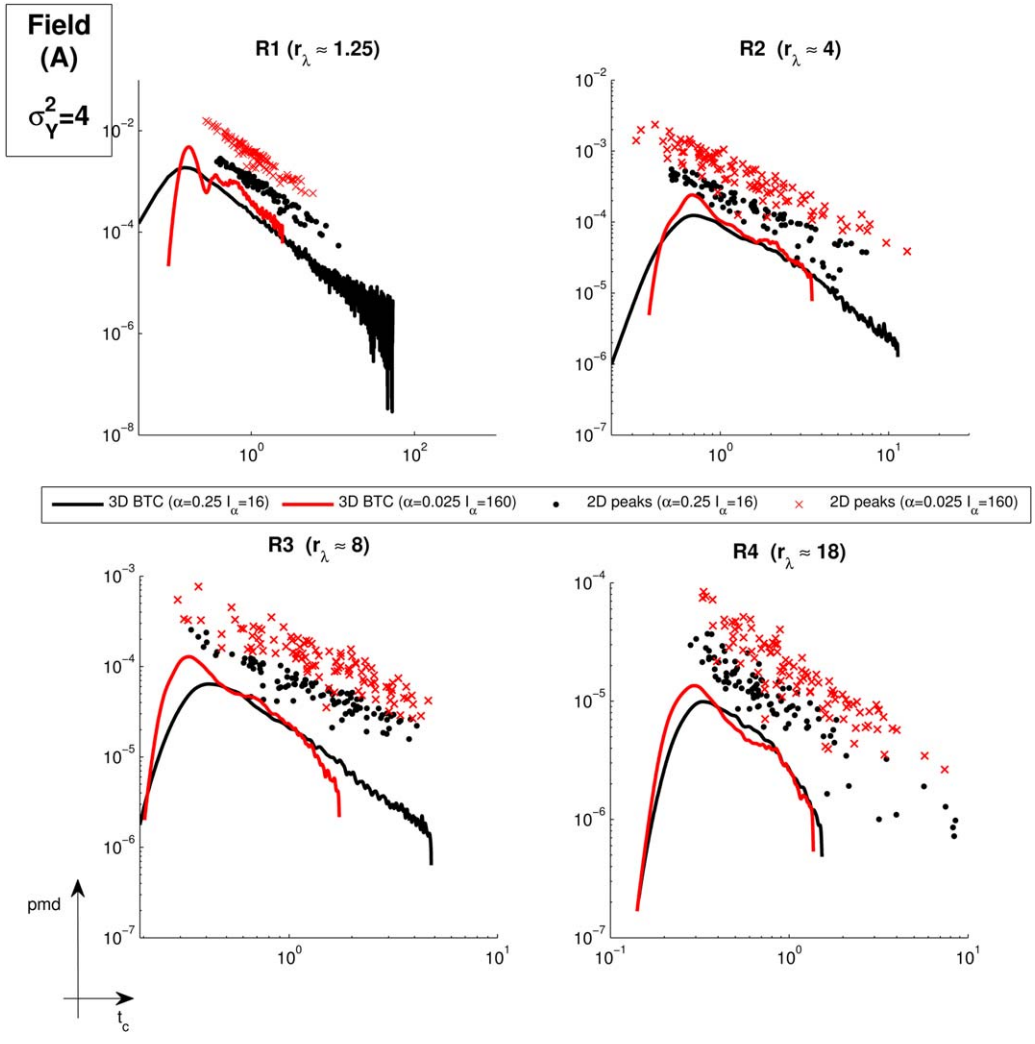

Figure 11. Comparison between 3-D BTCs (and relative peak distributions) obtained after injecting in the isotropic field (A) with $\sigma_Y^2 = 4$ at R points, with two different local dispersivity (α) values and consequently with two different I_α ratios.

injection column, and (b) the mean travel time along each horizon.

[99] In a perfectly stratified homogeneous medium ($e = I_z/I_x \rightarrow 0$), each layer acts independently. This is strictly valid assuming negligible transverse dispersion. In this limit case, convergent radial transport in each layer can be approximated by the analytical solution of *Welty and Gelhar* [1994, equation 26], which after some manipulation, allows us to estimate the peak concentration (c_{pk}) as

$$c_{pk} = \frac{M}{2Qt_{pk}}\left(\frac{4}{3}\pi\frac{\alpha_L}{r}\right) \tag{10}$$

where α_L is the longitudinal dispersivity. This solution is valid for advection-dominated transport ($r/\alpha_L > 20$). This result highlights that the maximum concentration in each layer scales linearly with the layer-specific injected mass M and inversely with the discharge rate Q.

[100] For the 2-D BTCs, the injected mass in all realizations is equal. Thus, the peak concentrations are governed by Q and t_{pk}. The parameter Pe is constant for a given injection distance. Hence, from (10) we can say that

$$c_{pk}t_{pk} \sim \psi\frac{M}{Q} \tag{11}$$

where ψ is a constant. Note that this relationship can and is often used to design the total mass of solute tracer to be injected during experiments.

[101] Now, how do we translate this concept to our three-dimensional models and to depth-integrated BTCs? Assuming again a perfectly stratified homogeneous medium, for a given layer and due to boundary conditions (flux-averaged injection), the ratio M/Q should be constant. Thus, in each layer the condition

$$c_{pk} \sim t_{pk}^{-1} \tag{12}$$

should be satisfied. Under some conditions (that we identified to be controlled by the parameters σ_Y^2, σ_t^2, and r_λ), the

3-D solute transport becomes so highly stratified that each layer acts separately, and the final shape is eventually similar to a PL with $m = 1$ (independent of the statistical distribution of Y, and also despite the fact that the three-dimensional flow solution allows for transverse dispersion). The further away from these conditions, the more the solution deteriorates.

[102] This explains why we found a universal scaling PL with slope $m = 1$ only for certain fields, and why it is different than $m = 2$ proposed by the *Becker and Shapiro* [2003] model. Their universal BTCs with PL slope $m = 2$ were obtained as a convolution of single BTCs from individual channels plus the ADE; however, they assumed individual channels acting independently that in each channel M is proportional to the cube of the mean channel size, and also that the mean advection time was proportional to the square of the mean channel aperture. Here we do not have such conditions since our solution for single "channel" (horizon) follows *Welty and Gelhar* [1994] solution, as stated previously.

5. Conclusions

[103] We have studied the development of heavy-tailed BTCs in heterogeneous porous media using a numerical approach, based on single realizations of flow and transport in stochastic multi-Gaussian log-normal hydraulic conductivity fields. We used a three-dimensional approach under convergent radial flow, to reflect realistic conditions often used in real tracer tests. We note that despite this very practical application, the topic appears to have received relatively little attention in the literature to date.

[104] This work focused on the development of heavy-tailed BTCs, and in particular on the physical mechanisms that determine PL tails with unit slope at late time (i.e., after the concentration peak has elapsed), which have been observed in real tests.

[105] The first conclusion of this work was that in realistic three-dimensional settings, the late-time distribution of the concentrations observed in convergent flow field tracer tests is mainly controlled by the degree of stratification of the solute. For a given random field with well-defined geostatistical properties, different late-time behaviors are observed for BTCs obtained from different injection locations.

[106] We note that we observe BTC scaling at late time with unit slope PL behavior when the following conditions are met:

[107] (1) large vertical variability of the connectivity for the layers making up the 3-D formation;

[108] (2) disordered systems (with mid to high variance);

[109] (3) injection distance comparable with the planar horizontal integral scale of the heterogeneity.

[110] Conditions 1 and 2 are highly correlated. We demonstrated that a possible reason for this is that the maximum concentrations of BTCs under homogeneous flow conditions scale inversely with arrival time of the peak value. When these conditions were not or only partially fulfilled, BTCs no longer showed PL distribution, but they could still display heavy tailing.

[111] This work suggested that full three-dimensional models are required to reproduce skewed BTCs similar to the ones observed in field settings. Tailing does not naturally occur in our 2-D transport simulations. Based on all of this we hypothesized that the nature of memory functions for large-scale effective models of such systems will depend heavily on the vertical architecture and connectivity patterns between the injection location and the pumping well.

[112] **Acknowledgments.** We thank A. Bellin and two anonymous reviewers for their useful suggestions and criticisms that have sensibly helped to improve the quality of this manuscript. We also acknowledge the discussions with A. Fiori and F. P. J. de Barros on some aspects of this research. This work has been supported by the Spanish Ministry of Science and Innovation through the projects Consolider-Ingenio 2010 CSD2009-00065 and FEAR CGL2012–38120. D.P. acknowledges the funding provided by the Spanish Ministry of Education through the FPU-MED 2009 Scholarship program. D.B. was supported by NSF grant EAR-1113704.

References

Bear, J. (1972), *Dynamics of Fluids in Porous Media*, Elsevier, New York.

Becker, M., and A. M. Shapiro (2000), Tracer transport in fractured crystalline rock: Evidence of nondiffusive breakthrough tailing, *Water Resour. Res.*, *36*(7), 1677–1686, doi:10.1029/2000WR900080.

Becker, M., and A. M. Shapiro (2003), Interpreting tracer breakthrough tailing from different forced-gradient tracer experiment configurations in fractured bedrock, *Water Resour. Res.*, *39*(1), 1014, doi:10.1029/2001WR001190.

Bellin, A., and Y. Rubin (2004), On the use of peak concentration arrival times for the inference of hydrogeological parameters, *Water Resour. Res.*, *40*, W07401, doi:10.1029/2003WR002179.

Bianchi, M., C. Zheng, G. Tick, and S. Gorelick (2011), Investigation of small-scale preferential flow with a forced-gradient tracer test, *Ground Water*, *49*(4), 503–514, doi:10.1111/j.1745–6584.2010.00746.x.

Bijeljic, B., and M. J. Blunt (2006), Pore-scale modeling and continuous time random walk analysis of dispersion in porous media, *Water Resour. Res.*, *42*, W01202, doi:10.1029/2005WR004578.

Bohling, G. C., G. LIu, S. J. Knobbe, E. C. Reboulet, D. W. Hyndman, P. Dietrich, and J. J. Butler J.R. (2012), Geostatistical analysis of centimeter-scale hydraulic conductivity variations at the MADE site, *Water Resour. Res.*, *48*, W02525, doi:10.1029/2011WR010791.

Bolster, D., F. J. Valdes-Parada, T. Le Borgne, M. Dentz, and J. Carrera (2011), Mixing in confined stratified aquifers, *J. Contam. Hydrol.*, *120–121*, 198–212.

Carrera, J., X. Sanchez-Vila, I. Benet, A. Medina, G. Galarza, and J. Guimerà (1998), On matrix diffusion: Formulations, solution methods and qualitative effects, *Hydrogeol. J.*, *6*, 178–190.

Dagan, G. (1989), *Flow and Transport in Porous Formations*, Springer, Berlin.

Dentz, M., and B. Berkowitz (2003), Transport behavior of a passive solute in continuous time random walks and multirate mass transfer, *Water Resour. Res.*, *39*(5), 1111, doi:10.1029/2001WR001163.

Dentz, M., and D. Bolster (2010), Distribution-versus correlation-induced anomalous transport in quenched random velocity fields, *Phys. Rev. Lett.*, *105*, 244301, doi:10.1103/PhysRevLett.105.244301.

Fernàndez-Garcia, D. (2003), Scale-dependence of non-reactive and sorptive transport parameters estimated from radial and uniform flow tracer tests in heterogeneous formations: Experimental and numerical investigations, PhD dissertation, Colo. Sch. of Mines, Golden.

Fernàndez-Garcia, D., and X. Sanchez Vila (2011), Optimal reconstruction of concentrations, gradients and reaction rates from particle distributions, *J. Contam. Hydrol.*, *120–121*, 99–114.

Fernàndez-Garcia, D., T. H. Illangasekare, and H. Rajaram (2004), Conservative and sorptive forced-gradient and uniform flow tracer tests in a three-dimensional laboratory test aquifer, *Water Resour. Res.*, *40*, W10103, doi:10.1029/2004WR003112.

Fernàndez-Garcia, D., H. Rajaram, and T. H. Illangasekare (2005), Assessment of the predictive capabilities of stochastic theories in a three-dimensional laboratory test aquifer: Effective hydraulic conductivity and temporal moments of breakthrough curves, *Water Resour. Res.*, *41*, W04002, doi:10.1029/2004WR003523.

Fernàndez-Garcia, D., P. Trinchero, and X. Sanchez-Vila (2010), Conditional stochastic mapping of transport connectivity, *Water Resour. Res.*, *46*, W10515, doi:10.1029/2009WR008533.

Fiori, A., and I. Jankovic (2012), On preferential flow, channeling and connectivity in heterogeneous porous formations, *Math. Geol.*, *44*, 133–145, doi:10.1007/s11004-011-9365-2.

Fiori, A., I. Jankovic, and G. Dagan (2006), Modeling flow and transport in highly heterogeneous three-dimensional aquifers: Ergodicity, Gaussianity, and anomalous behavior: 2. Approximate semianalytical solution, *Water Resour. Res.*, *42*, W06D13, doi:10.1029/2005WR004752.

Flach, G. (2012), Relationship between dual-domain parameters and practical characterization data, *Ground Water*, *50*(2), 216–229.

Fogg, G. E. (1986), Groundwater-flow and sand body interconnectedness in a thick, multiple-aquifer system, *Water Resour. Res.*, *22*(5), 679–694, doi:10.1029/WR022i005p00679.

Gelhar, L., and M. A. Collins (1971), General analysis of longitudinal dispersion in nonuniform flow, *Water Resour. Res.*, *7*(6), 1511–1521.

Gomez-Hernandez, J. J., and X. H. Wen (1998), To be or not to be multi-Gaussian? a reflection on stochastic hydrogeology, *Adv. Water Resour.*, *21*(1), 47–61.

Gouze, P., T. Le Borgne, R. Leprovost, G. Lods, T. Poidras, and P. Pezard (2008), Non-Fickian dispersion in porous media: 1. Multiscale measurements using single-well injection withdrawal tracer tests, *Water Resour. Res.*, *44*, W06426, doi:10.1029/2007WR006278.

Harbaugh, A. W., E. R. Banta, M. C. Hill, and M. G. McDonald (2000), Modflow-2000, the U.S. geological survey modular ground-water model—User guide to modularization concepts and the ground-water flow process, U.S. Geol. Surv. Open File Rep. 00–92, 121 pp.

Hoehn, E., J. Eikenberg, T. Fierz, W. Drost, and E. Reichlmayr (1998), The Grimsel migration experiment: Field injection-withdrawal experiments in fractured rock with sorbing tracers, *J. Contam. Hydrol.*, *34*, 85–106.

Knudby, C., and J. Carrera (2006), On the relationship between indicators of geostatistical, flow and transport connectivity, *Adv. Water Resour.*, *28*(4), 405–421, doi:10.1016/j.advwatres.2004.09.001.

Le Borgne, T., M. Dentz, D. Bolster, J. Carrera, J. R. de Dreuzy, and P. Davy (2010), Non-Fickian mixing: Temporal evolution of the scalar dissipation rate in heterogeneous porous media, *Adv. Water Resour.*, *33*(12), 1468–1475.

Levy, M., and B. Berkowitz (2003), Measurement and analysis of non-Fickian dispersion in heterogeneous porous media, *J. Contam. Hydrol.*, *64*(3–4), 203–226.

MacKay, D. M., D. L. Freyberg, P. V. Roberts, and J. A. Cherry (1986), A natural gradient experiment on solute transport in a sand aquifer: 1. Approach and overview of plume movement, *Water Resour. Res.*, *22*(13), 2017–2029, doi:10.1029/WR022i013p02017.

McKenna, S., L. Meigs, and R. Haggerty (2001), Tracer tests in a fractured dolomite: 3. Double-porosity, multiple-rate mass transfer processes in convergent flow tracer tests, *Water Resour. Res.*, *37*(5), 1143–1154, doi:10.1029/2000WR900333.

Moench, A. (1989), Convergent radial dispersion: A Laplace transform solution for aquifer tracer testing, *Water Resour. Res.*, *25*(3), 439–447, doi:10.1029/WR025i003p00439.

Parker, J. C., and M. T. Van Genuchten (1984), Flux-averaged and volume-averaged concentrations in continuum approaches to solute transport, *Water Resour. Res.*, *20*(7), 866–872, doi:10.1029/WR020i007p00866.

Ptak, T., and G. Schmid (1996), Dual-tracer transport experiments in a physically and chemically heterogeneous aquifer material: Effective transport parameters and spatial variability, *J. Hydrol.*, *183*(1–2), 117–138.

Ptak, T., M. Piepenbrink, and E. Martac (2004), Tracer tests for the investigation of heterogeneous porous media and stochastic modelling of flow and transport—A review of some recent developments, *J. Hydrol.*, *294*, 122–163.

Remy, N., A. Boucher, and J. Wu (2009), *Applied Geostatistics With SGeMS. A User's Guide*, Cambridge Univ. Press, New York.

Renard, P., and D. Allard (2013), Connectivity metrics for subsurface flow and transport, *Adv. Water Resour.*, *51*, 168–196, doi:10.1016/j.advwatres.2011.12.001.

Riva, M., A. Guadagnini, D. Fernandez-Garcia, X. Sanchez-Vila, and T. Ptak (2008), Relative importance of geostatistical and transport models in describing heavily tailed breakthrough curves at the Lauswiesen site, *J. Contam. Hydrol.*, *101*, 1–13, doi:10.1016/j.jconhyd.2008.07.004.

Salamon, P., D. Fernàndez-Garcia, and J. Gomez-Hernandez (2006), Modeling mass transfer processes using random walk particle tracking, *Water Resour. Res.*, *42*, W11417, doi:10.1029/2006WR004927.

Salamon, P., D. Fernàndez-Garcia, and J. Gomez-Hernandez (2007), Modeling tracer transport at the made site: The importance of heterogeneity, *Water Resour. Res.*, *43*, W08404, doi:10.1029/2006WR005522.

Sanchez-Vila, X., and J. Carrera (2004), On the striking similarity between the moments of breakthrough curves for a heterogeneous medium and a homogeneous medium with a matrix diffusion term, *J. Hydrol.*, *294*(1–3), 164–175, doi:10.1016/j.jhydrol.2003.12.046.

Sanchez-Vila, X., J. Carrera, and J. Girardi (1996), Scale effects in transmissivity, *J. Hydrol.*, *183*(1–2), 1–22.

Trinchero, P., X. Sanchez-Vila, and D. Fernàndez-Garcia (2008), Point-to-point connectivity, an abstract concept or a key issue for risk assessment studies?, *Adv. Water Resour.*, *31*(12), 1742–1753, doi:10.1016/j.advwatres.2008.09.001.

Welty, C., and L. W. Gelhar (1994), Evaluation of longitudinal dispersivity from nonuniform flow tracer tests, *J. Hydrol.*, *153*(1), 71–102.

Willmann, M., J. Carrera, and X. Sanchez-Vila (2008), Transport upscaling in heterogeneous aquifers: What physical parameters control memory functions?, *Water Resour. Res.*, *44*, W12437, doi:10.1029/2007WR006531.

Zinn, B., and C. F. Harvey (2003), When good statistical models of aquifer heterogeneity go bad: A comparison of flow, dispersion and mass transfer in connected and multivariate Gaussian hydraulic conductivity fields, *Water Resour. Res.*, *39*(3), 1051, doi:10.1029/2001WR001146.